Born reflection kernel analysis and wave equation reflection traveltime inversion in elastic media
Tengfei Wang and Jiubing Cheng, Tongji University

SUMMARY

Elastic reflection waveform inversion (ERWI) utilize the reflections to update the low and intermediate wavenumbers in the deeper part of model. However, ERWI suffers from the cycle-skipping problem due to the objective function of waveform residual. Since traveltime information relates to the background model more linearly, we use the traveltime residuals as objective function to update background velocity model using wave equation reflected traveltime inversion (WERTI). The reflection kernel analysis shows that mode decomposition can suppress the artifacts in gradient calculation. We design a two-step inversion strategy, in which PP reflections are firstly used to invert P wave velocity (V_p), followed by S wave velocity (V_s) inversion with PS reflections. P/S separation of multi-component seismograms and spatial wave mode decomposition can reduce the nonlinearity of inversion effectively by selecting suitable P or S wave subsets for hierarchical inversion. Numerical example of Sigsbee2A model validates the effectiveness of the algorithms and strategies for elastic WERTI (E-WERTI).

INTRODUCTION

With the development of high-performance computational abilities, people are paying more attention to the elastic full waveform inversion (EFWI) to recover the elastic properties of the subsurface (Vigh et al., 2014). EFWI provides high-resolution model estimation but notoriously surfers from the same nonlinearities or cycle-skipping problems as in acoustic case and also the trade-offs of multi-parameter inversion (Operto et al., 2013). In the absence of low frequency data and/or good initial models, EFWI falls into local minimal easily because of its incapability to recover the low and intermediate wavenumber components of the model.

Xu et al. (2012) suggested using a reflection waveform inversion (RWI) method to suppress the nonlinearity in FWI, which aim to invert the long-wavelength components of the model by using the reflections predicted by migration/demigration process. RWI highly relies on the accurate reflectivity to generate the reflections that can match the observed data. However, it is very challenging and also expensive to obtain a good reflectivity model through least-square migration when initial model is far away from the true value. Through minimizing misfit function of waveform in data domain, the RWI method is developed by several works (Wu and Alkhalifah, 2015; Zhou et al., 2015), and recently extended to elastic case by Guo and Alkhalifah (2016). The misfit function also can be built in image domain in the manner of wave equation migration velocity analysis (WEMVA), which tries to maximize energy at zero offset location in the extended image space (Biondi and Almomin, 2012; Sun and Symes, 2012). Raknes and Weibull (2016) developed the image-domain method in the 3D elastic media. Wang et al.

(2017) utilized PS image to update the V_s model through mode decomposition. But it is a big issue that the extended domain approach requires huge computational cost, especially in 3D case.

Traveltime information are more sensitive and linearly related to the low-wavenumber components of the model. Therefore, traveltime inversion will be more robust and helpful to build initial models containing long-wavelength components for conventional FWI (Chi et al., 2015; Luo et al., 2016). Ma and Hale (2013) introduced a wave equation reflected traveltime inversion (WERTI) method to build the low wavenumber of the model. Unfortunately, in elastic case, traveltimes of a particular wave mode are difficult to extract due to the complicated mode-conversions. The multi-parameter trade-offs will increase the nonlinearity as well. Wang and Cheng (2017) obtained good results by utilizing the wave mode decomposition to precondition the gradients in EFWI. The mode decomposition has been proved an efficient tool to provide decomposed data for hierarchical strategies.

We calculate the reflection wavepath and its components of different wave modes in elastic media. The investigation of reflection wavepath (kernel) shows the effectiveness of mode decomposition to suppress the artifacts in the gradient calculation. P/S separation of multicomponent seismograms is applied to the observed and predicted reflection data to extract the individual traveltime residuals through DIW (Hale, 2013). Based on the analysis of elastic reflection kernels and the separated traveltime residuals, we design a two-stage workflow to implement the E-WERTI method, in which the traveltime of PP is firstly used to recover the background V_p model followed by inverting the background V_s model through the traveltime of PS reflections. During the V_s inversion, we precondition the V_s gradient through spatial wave mode decomposition. Finally, the numerical example of Sigsee2A model proves the robustness and validity of our E-WERTI method.

METHOD

Objective function and gradients of elastic WERTI

Assume that there is a perturbation δc_{ijkl} in the background elastic media c_{ijkl}, the background wavefileds u_i and perturbed wavefields δu_i satisfy:

$$\rho \frac{\partial u_i^2}{\partial t^2} - \frac{\partial}{\partial x_j}\left[c_{ijkl} \frac{\partial u_k}{\partial x_l} \right] = f_i, \qquad (1)$$

and

$$\rho \frac{\partial \delta u_i^2}{\partial t^2} - \frac{\partial}{\partial x_j}\left[c_{ijkl} \frac{\partial \delta u_k}{\partial x_l} \right] = \frac{\partial}{\partial x_j}\left[\delta c_{ijkl} \frac{\partial u_k}{\partial x_l} \right], \qquad (2)$$

where δu_i can be seen as the demigrated reflection data using the image perturbation δc_{ijkl} obtained from RTM or other imaging method. In WERTI, we aim to minimize the traveltime

differences between observed data $\mathbf{d}^o$ and calculated data $\mathbf{d}^c$, then the objective function is:

$$\begin{cases} \tau(\mathbf{x_r}, t; \mathbf{x_s}) = \arg\min_{\tau} \| \mathbf{d}^c(\mathbf{x}_r, t; \mathbf{x}_s) - \mathbf{d}^o(\mathbf{x}_r, t+\tau; \mathbf{x}_s) \|^2 \\ E = \dfrac{1}{2} \int \tau^2(\mathbf{x_r}, t; \mathbf{x_s}) dt d\mathbf{x_r} d\mathbf{x_s}, \end{cases}$$
(3)

where the time differences $\tau(\mathbf{x_r}, t; \mathbf{x_s})$ can be extracted through DIW. After a similar derivation as in Ma and Hale (2013), the gradients of equation (3) can be expressed as:

$$\frac{\partial E}{\partial c_{ijkl}} = -\int \left(\frac{\partial u_i}{\partial x_j} \frac{\partial \delta \psi_k}{\partial x_l} + \frac{\partial \delta u_i}{\partial x_j} \frac{\partial \psi_k}{\partial x_l} \right),$$
(4)

where ψ_i and $\delta \psi_i$ are the adjoint wavefields satisfying:

$$\rho \frac{\partial \psi_i^2}{\partial t^2} - \frac{\partial}{\partial x_j} \left[c_{ijkl} \frac{\partial \psi_k}{\partial x_l} \right] = \tau(\mathbf{x_r}, t; \mathbf{x_s}) \frac{\dot{d}_i^o(\mathbf{x_r}, t+\tau; \mathbf{x_s})}{h_i(\mathbf{x_r}, t; \mathbf{x_s})},$$
(5)

and

$$\rho \frac{\partial \delta \psi_i^2}{\partial t^2} - \frac{\partial}{\partial x_j} \left[c_{ijkl} \frac{\partial \delta \psi_k}{\partial x_l} \right] = \frac{\partial}{\partial x_j} \left[\delta c_{ijkl} \frac{\partial \psi_k}{\partial x_l} \right],$$
(6)

with $h_i(\mathbf{x_r}, t) = \dot{d}_i^o(\mathbf{x_r}, t+\tau)^2 - \ddot{d}_i^o(\mathbf{x_r}, t+\tau)(d_i^c(\mathbf{x_r}, t) - d_i^o(\mathbf{x_r}, t+\tau))$. The hat dot denotes the time derivative. On the right hand side (RHS) of equation (4), the first and second term indicate the source and receiver part of the reflection wavepath, respectively. Then we can get the gradients in terms of P- and S- wave velocities through the chain rule:

$$\begin{aligned} \frac{\partial E}{\partial V_p} &= 2\rho V_p \frac{\partial E}{\partial c_{ijkl}} \delta_{ij}\delta_{kl}, \\ \frac{\partial E}{\partial V_s} &= 2\rho V_s \frac{\partial E}{\partial c_{ijkl}} (-2\delta_{ij}\delta_{kl} + \delta_{ik}\delta_{jl} + \delta_{il}\delta_{jk}). \end{aligned}$$
(7)

Elastic Born reflection kernel analysis

The key point of reflection inversion is to calculate the reflection kernel. RWI and WERTI utilize different objective functions which only induce different types of adjoint sources, but share similar reflection kernels. Due to the complex mode conversions in elastic wavefields, wavepath of elastic reflections will be far more complicated than that in acoustic case. Here, we decompose the origin kernel into four components which represent cross-correlation of different wave modes.

For simplicity, we rewrite (4) as follow:

$$\nabla E(\mathbf{m}_0) = -\int (\mathbf{u} \cdot \delta \boldsymbol{\psi} + \delta \mathbf{u} \cdot \boldsymbol{\psi})$$
(8)

with $\mathbf{u}$ and $\boldsymbol{\psi}$ are the forward and adjoint background wavefields, $\delta \mathbf{u}$ and $\delta \boldsymbol{\psi}$ are the forward and adjoint perturbed wavefields. The operator $\cdot$ denotes the cross correlation between two wavefields. Note that, equation (8) just schematically shows the manner of cross correlation. The detailed formulas should be derived according to the parameter $\mathbf{m}_0$ through chain rule, just as equation (7). Considering mode decomposition, the above formula can be decomposed into four types with:

$$K_{m_0}^{MN} = -\int (\mathbf{u}^M \cdot \delta \boldsymbol{\psi}^N + \delta \mathbf{u}^M \cdot \boldsymbol{\psi}^N),$$
(9)

where $m_0 \in \{V_p, V_s\}$ and $M, N \in \{P, S\}$. $K_{m_0}^{MN}$ represents the cross correlation between the M mode forward wavefields and the N mode adjoint wavefields. Note, it does not denote the kernel of MN mode data. For example, the reflection kernel of PS data should be $(\mathbf{u}^P \cdot \delta \boldsymbol{\psi}^P + \delta \mathbf{u}^S \cdot \boldsymbol{\psi}^S)$ but not K^{PS}.

To analyze the elastic reflection kernels, we calculate them with the single-source-receiver data which are synthesized by single reflector with pure P-wave source. In the first model, we place a single V_p reflector in the homogeneous background (Fig 1a and b). Since there is no perturbation of V_s, only PP reflection exist in the data, which is almost the same as in acoustic media. As shown in Figure 1c and d, the reflection kernel consists of two "rabbit-ear", the source and receiver parts. We can see the migration impulse below the reflector due to the down-going perturbed wavefields (Zone D mentioned by Zhou et al. (2015)). The energy in V_s kernel focus on the edge of the wavepath rather than the first Fresnel-Zone as in the V_p kernel. One plausible reason is that the V_s kernel is relatively insensitive to the PP data generated by V_p reflector.
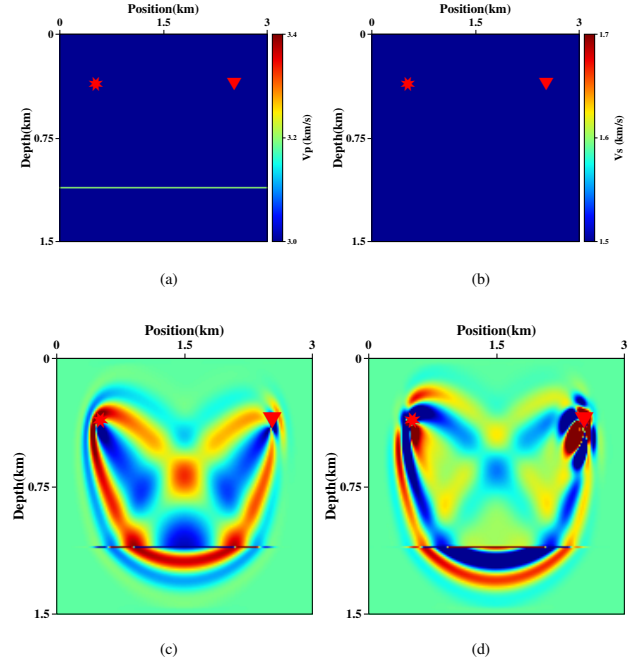

Figure 1: Kernels with single reflector in V_p model. (a) V_p model, (b) V_s model, (c) K_{V_p}, (d) K_{V_s}.

In the second model, we use the V_s reflector (Fig 2a and b) to generate both PP and PS reflection. The V_p kernel excludes S-wavefield automatically because of the divergence operator implied in the term $\delta_{ij}\delta_{kl}$ (equation (7)). However, $\delta \boldsymbol{\psi}$ contains the non-physical converted SP wavefields generated by the back-propagated $\boldsymbol{\psi}^S$ at the location of reflector. These SP wavefields make the V_p kernel slightly different from that in Figure 1c. If we only back-propagate the PP data, V_p kernel will be the same as Figure 1c.

For V_s kernel (Figure 2d), due to mode conversions, multi-

wavepaths overlapping with each other make it much more complicated and difficult to find the correct PS reflection kernel. The straightforward utilization of this kernel in gradient calculation will very likely cause severe cross-talk during reflection inversion. According to equation (9), we calculate the components of K_{V_s}, as shown in Figure 3. The $K_{V_s}^{PP}$ is similar to $K_{V_p}^{PP}$ but with an opposite sign. $K_{V_s}^{PS}$ and $K_{V_s}^{SP}$ mainly consist of high-wavenumber energy, which in fact are the migration impulse of cross-mode wavefields. Most importantly, we expect to update the V_s model through the S-wavepath in PS reflection, while $K_{V_s}^{SS}$ (Figure 33d) is exactly what we want. Therefore, we recommend using $K_{V_s}^{SS}$ to mitigate the cross-talks in V_s gradient calculation.
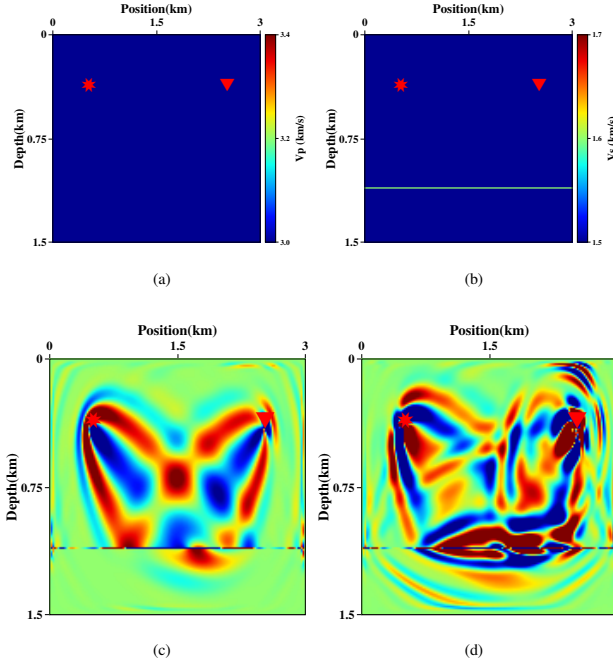

Figure 2: Kernels with single reflector in V_s model. (a) V_p model, (b) V_s model, (c) K_{V_p}, (d) K_{V_s}.

Workflow of elastic WERTI

DIW extracts the reflection traveltime differences in data domain. In elastic case, the cross points between different mode-conversions would be singularities for DIW. Therefore, $\tau(\mathbf{x_r}, t; \mathbf{x_s})$ would be inaccurate if using the original multicomponent seismic data, which makes equation (7) difficult to implement. Besides, according to the reflection kernel analysis, individually injecting PP or PS recordings also can mitigate the cross-talk in gradient calculation. Thus, we decompose the observed and calculated data into P- and S-wave parts through P/S separation of multi-component seismograms (Li et al., 2016). In this way, the traveltime differences can be decoupled into P- and S-wave part, with which we can implement the elastic WERTI through a two-stage workflow, i.e. the P-wave stage followed by the S-wave stage.

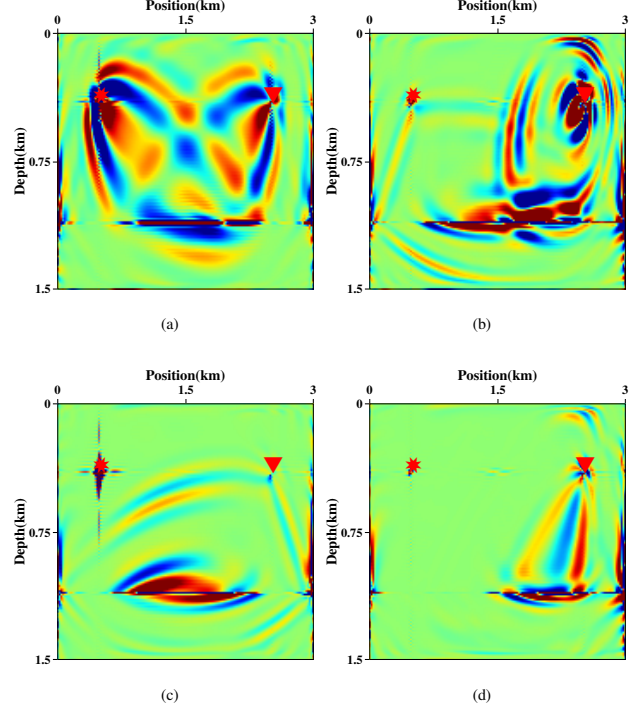In the first stage, we use PP traveltime to recover V_p model.

Figure 3: Four components of K_{V_s}. (a) $K_{V_s}^{PP}$, (b) $K_{V_s}^{PS}$, (c) $K_{V_s}^{SP}$, (d) $K_{V_s}^{SS}$.

Since only the traveltime is considered in WERTI, just ERTM is applied to obtain the image rather than in a least-square manner (LSRTM) to find the correct reflectivity. Therefore, the objective function is:

$$E_{PP} = \frac{1}{2} \int \tau_{pp}^2(\mathbf{x_r}, t; \mathbf{x_s}) dt d\mathbf{x_r} d\mathbf{x_s}. \quad (10)$$

Thus, we can obtain the gradient of V_p ($\frac{\partial E}{\partial V_p}$), just using the P-wave seismograms to calculate RHS of equation (5) and replacing δc_{ijkl} with δV_p in equation (2) and (6).

In the S-wave stage, the objective function becomes:

$$E_{ps} = \frac{1}{2} \int \tau_{ps}^2(\mathbf{x_r}, t; \mathbf{x_s}) dt d\mathbf{x_r} d\mathbf{x_s}. \quad (11)$$

However, the implementation is a little different from the previous stage. After the P-wave stage inversion, the background V_p should be well recovered. As we know, in most cases V_p and V_s share the same structure in the subsurface. Therefore, we recommend to use the well imaged δV_p instead of δV_s to generate the PS reflections. Besides, in order to make sure that reflected S-wavepath is used to update V_s, wave mode decomposition is implemented to calculate $K_{V_s}^{SS}$ with:

$$\frac{\partial E_{ps}}{\partial V_s} = -2\rho V_s \int (\frac{\partial \delta u_i^S}{\partial x_j} \frac{\partial \psi_k^S}{\partial x_l})(\delta_{ik}\delta_{jl} + \delta_{il}\delta_{jk}). \quad (12)$$

This is similar to the gradient precondtioning for EFWI proposed by Wang and Cheng (2017). The mode decomposition can mitigate parameter trade-offs and suppress artifacts for the V_s inversion.
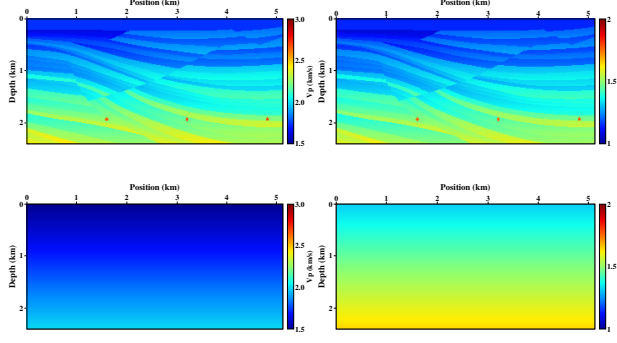
Figure 4: Sigbee2A model example. On the top are true models of V_p (a) and V_s (b). On the bottom are initial models of V_p (c) and V_s (d) linearly increasing with depth.

NUMERICAL EXAMPLE

We select a part of the Sigsbee2A model (Figure 4a and 4b) to test the inversion algorithm and strategy. The V_s model is generated using fixed Poisson's ratio. The initial model for E-WERTI are shown in Figure 4c and 4d. The linearly increasing initial model of V_p is generally lower while V_s is higher than the true model, and both of them are far from the true value. 36 shots are evenly deployed on the surface and receivers are fixed with a maximum offset of 4km. The main frequency of P-wave source is 15Hz.

Figure 5a and 5b show the inverted results of E-WERTI. After 40 iterations for each stage, WERTI provides a good recovery of the background information for both V_p and V_s. Nonetheless, on the right part, the reflection coverage of surface observation is insufficient for WERTI to rebuild the long-wavelength components. Using the inverted results of WERTI as starting models, we also perform the conventional EFWI. As shown in Figure 5c and 5d, both of the inverted V_p and V_s models are well reconstructed except the right part.

CONCLUSIONS

Reflection traveltime inversion only minimizes traveltime misfits which are more sensitive and linearly related to the low-wavenumber model perturbation. The kernel analysis of different wave modes show that mode decomposition can suppress artifacts and recover the correct reflection wavepath in gradient calculation. With the aid of DIW and P/S separation of 3C seismograms, we can obtain the travel time differences of PP and PS reflections, respectively. To build the long-wavelength component of the model, we introduce a two-stage WERTI workflow by firstly using PP then PS reflections, through which the non-linearity of reflection inversion is reduced effectively. In the second stage, the wave mode decomposition is introduced to calculate the gradient of V_s to mitigate the trade-off between V_p and V_s. The Sigbee2A model example shows that even starting with a bad initial model, the two-stage E-WERTI can provide reliable starting model for conventional EFWI.
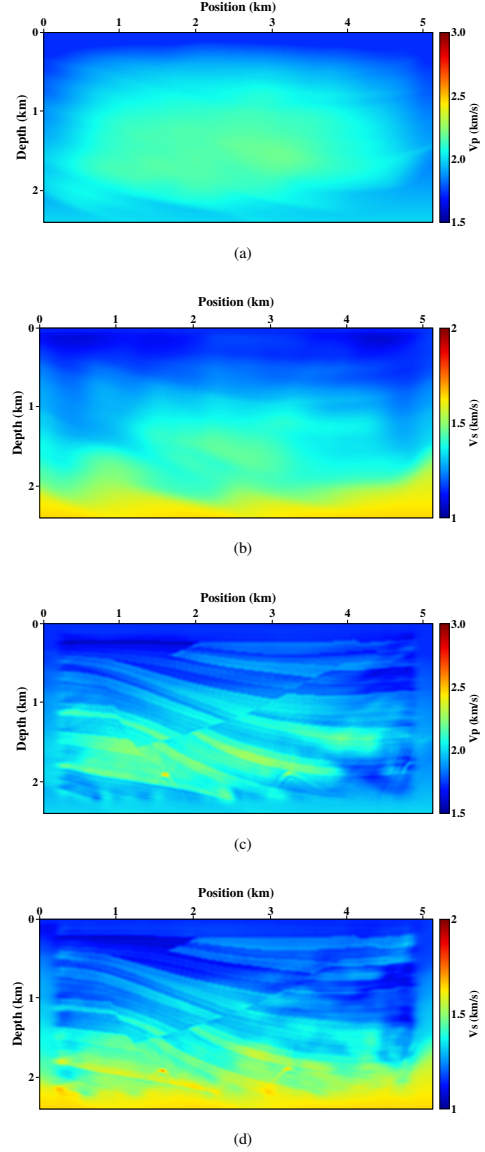

(a)

(b)

(c)

(d)

Figure 5: Inverted results of WERTI and EFWI. (a) and (b) are inverted V_p and V_s model through two-stage elastic WERTI with the linearly increased models as initial models. (c) and (d) are inverted V_p and V_s through EFWI using (a) and (b) as starting models.

REFERENCES

Biondi, B., and A. Almomin, 2012, Tomographic full waveform inversion (TFWI) by combining full waveform inversion with wave-equation migration velocity anaylisis, *in* SEG Technical Program Expanded Abstracts 2012: Society of Exploration Geophysicists.

Chi, B., L. Dong, and Y. Liu, 2015, Correlation-based reflection full-waveform inversion: Geophysics, **80**, R189–R202.

Guo, Q., and T. Alkhalifah, 2016, *in* A nonlinear approach of elastic reflection waveform inversion: Society of Exploration Geophysicists, 1421–1425.

Hale, D., 2013, Dynamic warping of seismic images: Geophysics, **78**, S105–S115.

Li, Z., X. Ma, C. Fu, B. Gu, and G. Liang, 2016, Frequency-wavenumber implementation for p- and s-wave separation from multi-component seismic data: Exploration Geophysics, **47**, 32.

Luo, Y., Y. Ma, Y. Wu, H. Liu, and L. Cao, 2016, Full-traveltime inversion: Geophysics, **81**, R261–R274.

Ma, Y., and D. Hale, 2013, Wave-equation reflection traveltime inversion with dynamic warping and full-waveform inversion: Geophysics, **78**, R223–R233.

Operto, S., Y. Gholami, V. Prieux, A. Ribodetti, R. Brossier, L. Metivier, and J. Virieux, 2013, A guided tour of multiparameter full-waveform inversion with multicomponent data: From theory to practice: The Leading Edge, **32**, 1040–1054.

Raknes, E. B., and W. Weibull, 2016, Combining wave-equation migration velocity analysis and full-waveform inversion for improved 3D elastic parameter estimation, *in* SEG Technical Program Expanded Abstracts 2016: Society of Exploration Geophysicists.

Sun, D., and W. W. Symes, 2012, Waveform inversion via non-linear differential semblance optimization, *in* SEG Technical Program Expanded Abstracts 2012: Society of Exploration Geophysicists.

Vigh, D., K. Jiao, D. Watts, and D. Sun, 2014, Elastic full-waveform inversion application using multicomponent measurements of seismic data collection: Geophysics, **79**, R63–R77.

Wang, C., W. Weibull, J. Cheng, and B. Arntsen, 2017, Automatic shear-wave velocity analysis with elastic reverse time migration: 79th EAGE Conference and Exhibition 2017, Expanded Abstracts.

Wang, T., and J. Cheng, 2017, Elastic full waveform inversion based on mode decomposition: the approach and mechanism: Geophysical Journal International, **209**, 606–622.

Wu, Z., and T. Alkhalifah, 2015, Simultaneous inversion of the background velocity and the perturbation in full-waveform inversion: Geophysics, **80**, R317–R329.

Xu, S., D. Wang, F. Chen, G. Lambare, and Y. Zhang, 2012, Inversion on reflected seismic wave: 82nd Annual International Meeting, SEG, Expanded Abstracts, 1–7.

Zhou, W., R. Brossier, S. Operto, and J. Virieux, 2015, Full waveform inversion of diving & reflected waves for velocity model building with impedance inversion based on scale separation: Geophysical Journal International, **202**, 1535–1554.